Journal of Materials Chemistry C

REVIEW

View Article Online
View Journal | View Issue

Cite this: J. Mater. Chem. C, 2015, 3, 11999

Received 13th September 2015,
Accepted 14th October 2015

DOI: 10.1039/c5tc02886h

www.rsc.org/MaterialsC

Bismuth nanowire thermoelectrics

Jeongmin Kim, Wooyoung Shim* and Wooyoung Lee*

During the past 20 years, the thermoelectric properties of nanostructures such as one-dimensional bismuth (Bi) platforms have prompted the development of a wide variety of nanowire growth methods, aiming to achieve higher energy-conversion efficiency. Most of these methods have demonstrated single-crystal nanowire growth of a quality unmatched in bulk Bi. However, in contrast to the theoretical expectation that Bi nanowires should exhibit high thermoelectric performance, their observed thermoelectric properties have prevented their technological exploitation. Here, we review the current progress in the thermoelectrics of bismuth nanowires, the fundamentals of their advantage and limitation over bulk Bi, and their potential use for enhancing the thermoelectric performance.

1. Introduction

1.1 Low-dimensional thermoelectrics

The thermoelectric efficiency of a single material can be determined independently of the sample size using a dimensionless thermoelectric figure of merit $ZT = \sigma S^2 T/\kappa$,[1] expressed in terms of the electrical conductivity σ, Seebeck coefficient S, absolute temperature T, and thermal conductivity κ. Here, the power factor (σS^2) and κ indicate the electrical and thermal thermoelectric performance, respectively. Although this quantity correlates with the suitability of the thermoelectric effect for applications in principle, its value for commercial thermoelectric materials so far does not exceed 1.0 at room temperature.[2] This limitation is due to the nature of the materials. In general, it is very difficult to control the thermoelectric properties (σ, S, and κ) independently,[2,3] because σ and S are in a trade-off relationship depending on the carrier concentration n.[4] To treat the n-dependency of the thermoelectric properties, a simple rigid band approximation is often employed.[5,6] In this approach, doping is simulated by moving the Fermi energy (E_F) level in a changeless band structure. The electrical conductivity increases with n according to Ohm's law, $\sigma = en\mu_d$, where e and μ_d are the charge of an electron and the carrier drift mobility, respectively. Therefore, in typical thermoelectric materials, a high level of doping (resulting in a deep-band E_F) yields a higher electrical conductivity than a

Department of Materials Science and Engineering, Yonsei University, 134 Shinchon, Seoul 120-749, Korea. E-mail: wooyoung@yonsei.ac.kr, wshim@yonsei.ac.kr

Jeongmin Kim

Jeongmin Kim obtained his BS degree in metallurgical engineering from the Yonsei University (Korea) in 2008. His PhD studies under the supervision of Prof. Wooyoung Lee in the Department of Materials Science and Engineering at the Yonsei University include galvanomagnetic and thermoelectric transport properties of low-dimensional materials. Throughout this time, his prime focus of research has been on studying and enhancing the thermoelectric performance of low-dimensional materials using nanowires based on bismuth.

Wooyoung Shim

Wooyoung Shim is an assistant professor at Yonsei University in Korea. He attended the Yonsei University for his undergraduate education and graduate program for his master degree in the Department of Materials Science and Engineering. After his doctoral studies at the Northwestern University and postdoctoral research at the Harvard University, he moved back to Yonsei in 2014 to assume the position of assistant Professor. At Yonsei, he has been interested in the synthesis of a broad range of nanoscale materials and the development of methods of hierarchical assembly of nanoscale materials, together with the development of nanolithographic tools for future nanotechnology-enabled sensors and related nanoelectronics.

low doping level (near-band-edge E_F). This is illustrated in Fig. 1(a). On the other hand, the absolute value of the Seebeck coefficient can be determined by Mott's formula, $S = -|(\pi^2 k_B^2 T/3e)\cdot(d \ln \sigma(E)/dE)|_{E_F}$, where k_B is the Boltzmann constant.[5,7] Thus, S is proportional to the rate of change in the density of states (DOS) with energy (dDOS/dE) near the Fermi energy. As shown in Fig. 1(a), in a bulk 3D crystalline semiconductor, S can be greater when the Fermi energy is at the band-edge instead of in a deep-band. Therefore, in this regard, a distorted band structure, which has a high curvature narrow DOS peak in a broad band, can be promising to enhance σ and S simultaneously.[5,6,8]

The distorted band structure is shown on the left-hand side of Fig. 1(b). A large DOS with a strong curvature near the Fermi level results in a large σ and a high S. Low-dimensional thermoelectric materials, with properties governed by quantum mechanics, can provide such a band structure. The right-hand side of Fig. 1(b) sketches the electronic DOS configurations for a 3D bulk material, a 2D quantum well, a 1D nanowire, and a 0D quantum dot. In each case, the shape of the DOS is dictated by the degree of confinement of the carriers imposed by the dimensionality. Among these, the DOS of the 1D nanowire most closely resembles the band structure required for enhancing thermoelectric performance.[3] A further benefit of 1D materials is their thermal transport properties. The overall thermal conductivity has two contributions: an electron thermal conductivity (κ_e) and a lattice thermal conductivity (κ_{ph}), which involve charge carriers (electrons and holes) and phonons as the heat carriers, respectively. Whereas κ_e is closely related to σ *via* the Wiedemann–Franz law (as heat and charge are transported by the same carriers), κ_{ph} can be reduced by the increase in phonon scattering originating from the lower dimensionality.[3,9]

Wooyoung Lee

Wooyoung Lee is a professor of the Department of Materials Science and Engineering and the Head of Institute of Nanoscience and Nanotechnology at the Yonsei University in Korea. He received a BS degree in metallurgical engineering in 1986, an MS degree in metallurgical engineering from the Yonsei University in 1988. He received a PhD degree in physics from the University of Cambridge, England, in 2000. In recent years, his research interests have centered on thermoelectric materials and devices, permanent magnets, hydrogen sensors and hydrogen storage materials. He has received a number of awards in nano-related research areas and a Service Merit Medal (2008) from the Korean Government due to his contribution to the development of intellectual properties. He has authored and co-authored over 150 publications, and has edited a few of special books on nano-structured materials and devices.

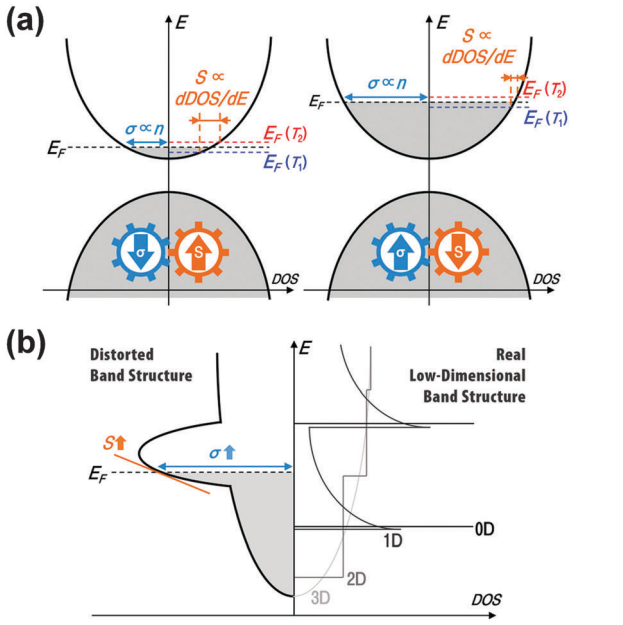

Fig. 1 Schematic DOS of thermoelectric materials. (a) For the DOS of a bulk crystalline thermoelectric material, the electrical conductivity and Seebeck coefficient are in a trade-off relationship depending on the level of doping (location of E_F). The electrical conductivity and Seebeck coefficient are proportional to the carrier concentration and the difference of the DOS in the cold (T_1) and hot (T_2) regions, respectively. The DOS difference per identical temperature difference gradually increases with E_F towards the band-edge. (b) The desired DOS structure for enhancing the thermoelectric performance is compared with the DOS in generic zero-, one-, two-, and three-dimensional materials.

It is for this reason that 1D structures have been considered as promising thermoelectric materials.

1.2 Historical review of Bi nanowires

Fig. 2 summarizes more than twenty years of intensive research into 1D nanostructures based on single-crystalline bismuth (Bi), aimed at demonstrating the enhancement of thermoelectric performance. Initial theoretical studies considered low-dimensional structures, such as quantum wells and nanowires, based on bismuth telluride and Bi (1993–2000).[10–13] The potential of Bi as a low-dimensional thermoelectric material stems from its unique properties. Semimetallic Bi has a highly anisotropic electronic band structure in the Brillouin zone (L-point conduction band and T-point valence band) and its band overlap energy is very small ($E_0 \sim 38$ meV).[13,14] Moreover, it has a small effective carrier mass ($m^* \sim 0.001$), a long mean free path ($l \sim 1$ mm), and a large Fermi wavelength ($\lambda_F \sim 70$ nm).[15–17] Thus, it is relatively convenient to control quantum confinement in a single-crystalline Bi nanowire, as compared to conventional materials, by decreasing its diameter. This effect can drive a semimetal-to-semiconductor (SMSC) transition that enhances thermoelectric efficiency.[12,13] A shift in the band structure was theoretically predicted to commence at a diameter just below 400 nm, leading to a SMSC transition below 50 nm.[13,17] The first experimental studies to demonstrate the enhancement of thermoelectric performance were done using

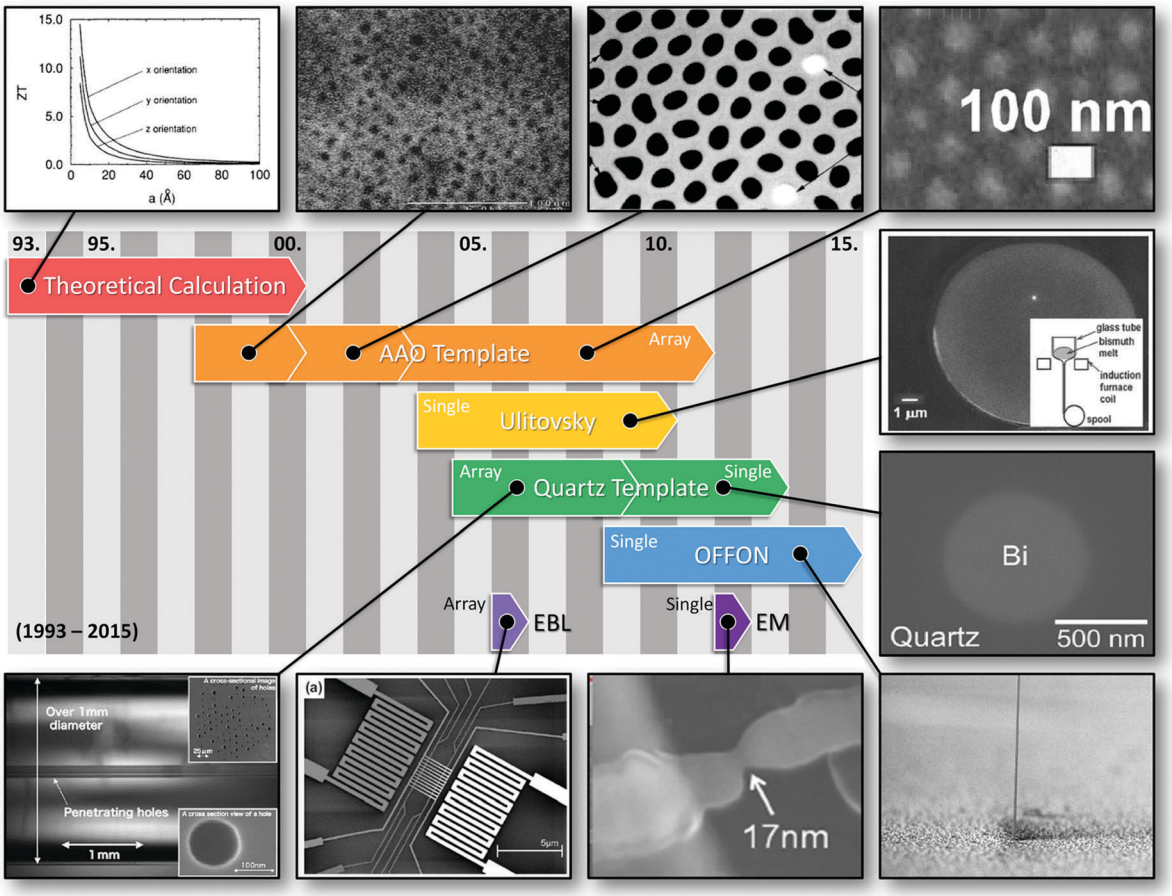

Fig. 2 Historical overview of research on Bi-nanowire thermoelectrics. The thermoelectric properties were measured from array- and single-type Bi nanowires. The array-type nanowires were grown by the AAO template, quartz template, and EBL methods. The single-type nanowires were grown by the Ulitovsky, quartz template, OFFON, and EM methods. Reprinted with permission from The American Physical Society,[11,16,27,30] Taylor & Francis,[24] Wiley-VCH Verlag GmbH,[39] Springer,[34] The American Institute of Physics,[37] and The American Chemical Society.[40,45]

single-crystalline Bi nanowires grown using anodic aluminum oxide (AAO) templates (1998–2000).[14,16,18–21] In these studies, temperature-dependent resistance,[16] magnetoresistance (MR),[14,18] optical properties,[19] and the Seebeck coefficient[20,21] of array-type single-crystalline Bi nanowires were intensively investigated. Moreover, another band-engineering approach for achieving a high Seebeck coefficient, referred to as "pocket engineering", was suggested theoretically based on Sn-doped Bi nanowire (2001).[22] This effect was confirmed experimentally using Sn-doped array-type single-crystalline Bi nanowires grown using AAO templates (2001–2003).[23–25] Separately, transport phenomena dominated by surface states were observed in the electrical conductance and Seebeck coefficient in Bi nanowires with a diameter below 50 nm.[26,27] These measurements were obtained from magneto-transport experiments including Shubnikov–de Haas (SdH) and Aharonov–Bohm oscillations, using both array-type and individual single-crystalline Bi nanowires grown using AAO templates (2004–2011)[27–29] and the Ulitovsky method (2004–2010),[26,30–32] respectively. At the same time, another growth method for single-crystalline Bi nanowires, involving pressurized injection using quartz templates, was investigated to allow the measurement of transport properties (including the Seebeck coefficient) in both array-type (2005–2009)[33–35] and individual (2010–2013)[36–38] Bi nanowires. In 2006, the variation in the Seebeck coefficient was demonstrated experimentally in a poly-crystalline Bi-nanowire array fabricated by electron-beam lithography (EBL), consistent with diameter reduction, despite the measured Seebeck coefficient being slightly smaller than in single-crystalline Bi nanowires.[39] In 2009, a stress-induced method to grow single-crystalline Bi nanowires, which is named "on-film formation of nanowires" (OFFON), was reported.[40] Using these nanowires, the variation in intrinsic properties due to quantum confinement, controlled by decreasing the diameter, was confirmed by magneto-transport measurements (2009–2014).[41–43] Moreover, since all the thermoelectric properties, including the electric conductivity, Seebeck coefficient, and thermal conductivity, were measured as a function of diameter, the diameter-dependent thermoelectric figure of merit could be determined (2015).[44] In 2012, the first significant increase in the Seebeck coefficient was observed.[45] In this study, although the low-dimensional Bi structure was more similar to a quantum point contact than a nanowire, the extremely narrow constriction was

achieved using the electromigration (EM) effect in Bi nanowires.

This review article summarizes the advances in low-dimensional thermoelectric materials based on Bi nanowires over the last twenty years, from the growth method of single-crystalline Bi nanowires to experimental measurements of their thermoelectric properties based on the fundamental properties of Bi, to assess the potential of Bi nanowire as a high-performance low-dimensional thermoelectric material.

2. Fundamental properties

2.1 Crystal structure

Rhombohedral bismuth can be described using several different lattice systems to emphasize various specific structural characteristics, as shown in Fig. 3(a)[17,46,47] Firstly, the crystal structure of Bi can be represented most simply as a rhombohedral lattice with two atoms per unit cell, with three-different lattice vectors, $\vec{a}_1$, $\vec{a}_2$, and $\vec{a}_3$ (red arrows in Fig. 3(a), left panel). The angle between these vectors is 57.23°. The second atom is located at approximately 0.48 × ($\vec{a}_1$ + $\vec{a}_2$ + $\vec{a}_3$), as shown in Fig. 3(a), left panel. Secondly, a hexagonal lattice system is conventionally used with $\vec{a}_1$, $\vec{a}_2$, $\vec{a}_3$, and $\vec{c}$ lattice vectors (blue arrows in Fig. 3(a), left panel). Although the angles between the $\vec{a}$ vectors equal 120° and they lie in the plane normal to the $\vec{c}$ vector, the fact that $|\vec{a}_1| = |\vec{a}_2| = |\vec{a}_3|$ allows a description in terms of three lattice vectors ($\vec{a}_1$, $\vec{a}_2$, and $\vec{c}$) and two different lattice parameters, a and c. Thirdly, a Cartesian coordinate system can also be used, with special rotational symmetry axes denoted trigonal, binary, and bisectrix (black arrows in Fig. 3(a), left panel). The trigonal axis, which has three-fold rotational symmetry, is aligned with the $\vec{a}_1$ + $\vec{a}_2$ + $\vec{a}_3$ direction and with the $\vec{c}$ direction in the rhombohedral and hexagonal lattices, respectively. The binary axis has two-fold rotational symmetry, which is same with the $\vec{a}$ direction in the hexagonal lattice. The bisectrix axis is defined as being orthogonal to the trigonal and binary axes. Finally, the anisotropic crystal structure of Bi can be understood easily using the pseudo-cubic lattice shown in Fig. 3(a), right panel. This lattice can be described as two interpenetrating face-centered cubic (FCC) lattices, displaced and stretched along the trigonal axis. Then, the lattice is distorted from a cubic owing to the displacement (to the 0.49 : 0.52 position) of the second atom; the angle between the primitive lattice vectors (57.23°) is slightly smaller than the value in a FCC (60°) as a result of the stretch. Although the cubic-like lattice is slightly distorted from a cubic owing to the migration and the stretch, the pseudo-cubic lattice clearly exhibits the stretched structure of Bi along the trigonal axis and explains well the anisotropic electronic band structure of Bi in momentum space.

2.2 Electronic band structure

The stretched crystal structure of Bi along the trigonal axis produces a highly anisotropic electronic band structure of the Brillouin zone in momentum space (Fig. 3(b)).[17,46–49] Whereas a cubic has four crystallographically identical diagonal directions,

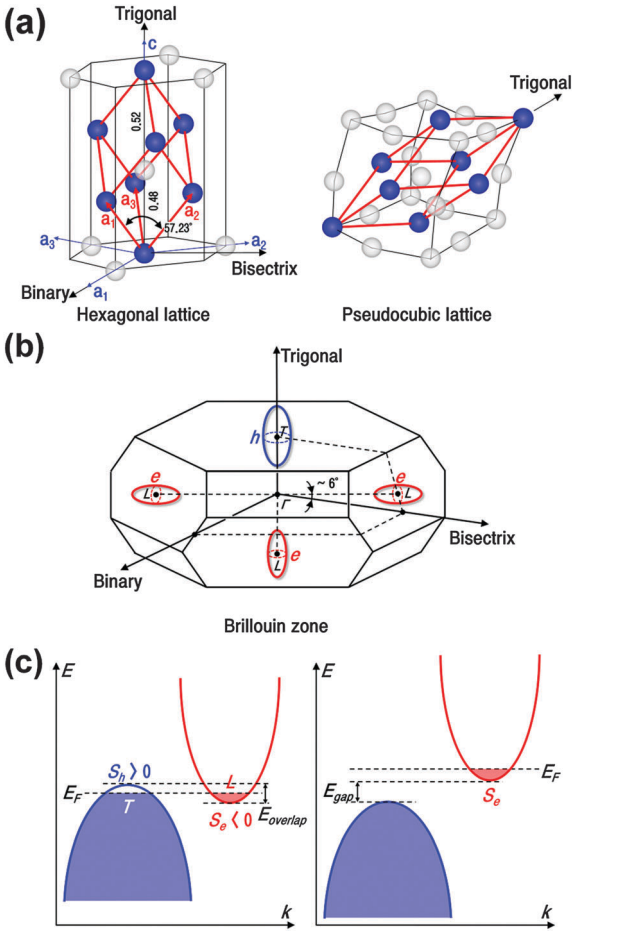

Fig. 3 Crystal and electronic band structure of bulk Bi. (a) Left: The crystal structure of Bi can be represented with the rhombohedral lattice vectors (red arrows), the hexagonal lattice vectors (blue arrows), and the Cartesian coordinate system (black arrows). Right: This structure also can be described as a pseudo-cubic lattice (black lines) with a rhombohedral unit cell (red lines). (b) One hole and three electron Fermi pockets in the Brillouin zone of bulk Bi. The three electron Fermi pockets are crystallographically identical, according to the rotational symmetry of the trigonal and binary axes. (c) Left: Electronic band structure of bulk Bi. The total Seebeck coefficient is calculated as the sum of the partial Seebeck coefficients of the T-point valence band and the L-point conduction band, weighted by their respective partial conductivities. Right: Schematics of band-gap opening by band engineering. The total Seebeck coefficient can be determined solely from each band without deep-band Fermi energy shifting, thanks to the band gap.

the pseudo-cubic lattice of Bi is stretched along one diagonal direction, which becomes the trigonal or c-axis in real space and forms the T-point of the Brillouin zone in momentum space. Although the three other diagonal directions lose the three-fold rotational symmetry as a result of the stretch and the displacement, they remain crystallographically identical and are denoted as the L-point of the Brillouin zone in momentum space. Consequently, Bi has one hole Fermi pocket and three identical electron Fermi pockets at the T- and L- points of the Brillouin zone, respectively. It can therefore be said that the crystal structure, stretched along the trigonal or c-axis in real space, compresses the Brillouin zone in the direction of the T-point,

giving an anisotropic band structure in momentum space as shown in Fig. 3(b).

In intrinsic Bi, the *T*-point valence band and the *L*-point conduction band overlap indirectly (38–98 meV at 2–300 K)[14,17,50–52] and the Fermi level is located between each band edge, producing semimetallic characteristics where electrons and holes coexist, as shown in Fig. 3(c), left panel. Because the Fermi level is located close to each band edge, the partial Seebeck coefficient of each subband should be large; its value for electron and hole subbands was calculated theoretically as $S_e = -486\ \mu V\ K^{-1}$ and $S_h = 669\ \mu V\ K^{-1}$, respectively.[20] Although the calculated partial Seebeck coefficients were significantly larger than typical metals and semiconductors, the total Seebeck coefficient of Bi remains relatively small, owing to the opposite sign of each partial Seebeck coefficient. In the two-band model, the total Seebeck coefficient can be expressed using the partial Seebeck coefficient of each subband weighted by the respective partial conductivity:

$$S_{total} = \frac{\sigma_e S_e + \sigma_h S_h}{\sigma_e + \sigma_h}. \quad (1)$$

Thus, the large partial Seebeck coefficients for the electrons and holes cancel to give a smaller total Seebeck coefficient. In practice, the Seebeck coefficient of Bi, which was measured experimentally, cannot exceed $\pm 100\ \mu V\ K^{-1}$. To enhance the total Seebeck coefficient, the contribution of minority carrier should be eliminated. This can be achieved by shifting the Fermi level deeper into the major band using the doping effect, but the large partial Seebeck coefficient of the major subband is then also reduced, as explained in Fig. 1(a). Consequently, to maintain and use the large partial Seebeck coefficient, the Fermi level should be located at the band edge without minority carriers, *i.e.*, the band gap between each subband is necessary, as shown in Fig. 3(c), right panel. This is a major motivation for achieving an enhancement of thermoelectric performance using low-dimensional Bi. The details of the theoretical prediction will be discussed below.

2.3 Theoretical calculation

As explained above, although the first theoretical predictions of the enhanced thermoelectric performance in low-dimensional materials were based on bismuth telluride, the calculation is valid for a metal, semiconductor, and semimetal, as long as it is one band material.[10,11] This enhancement was attributed to the dispersion relation associated with the confinement in a low-dimensional structure, which for a 1D quantum wire and assuming a simple parabolic band is given by[11,12]

$$E_{1D}(k_x) = \frac{\hbar^2 {k_x}^2}{2m_x} + \frac{\hbar^2\pi^2}{2m_y d^2} + \frac{\hbar^2\pi^2}{2m_z d^2}, \quad (2)$$

where $\hbar$, k, and d are the reduced Planck's constant, wavenumber, and diameter, respectively. The quantities m_x, m_y, and m_z are the effective mass-tensor components, on the assumption that the current and nanowire directions are along x and quantum confinement is imposed along y and z. According to eqn (2), the solutions of the Boltzmann equation were obtained for the thermoelectric properties (σ, S, and κ); hence, ZT is given by[11]

$$ZT = \frac{\frac{1}{2}\left(\frac{3F_{1/2}}{F_{-1/2}} - \eta\right)^2 F_{-1/2}}{\frac{1}{B} + \frac{5}{2}F_{3/2} - \frac{9{F_{1/2}}^2}{2F_{-1/2}}}, \quad (3)$$

where the Fermi Dirac functions F_i and B are

$$F_i = \int_0^\infty \frac{x^i dx}{e^{(x-\eta)} + 1}, \quad (4)$$

$$B = \frac{2}{\pi d^2}\left(\frac{2k_B T}{\hbar^2}\right)^{1/2} \frac{{k_B}^2 T {m_x}^{1/2}\mu_x}{e\kappa_{ph}}. \quad (5)$$

where $\eta = \zeta/k_B T$ is the reduced chemical potential and k_B is the Boltzmann constant. Therefore, the decrease in d leads to an increase in B monotonically resulting in the enhancement of ZT at an optimized η. Moreover, the decrease of κ_{ph} caused by the spatial restriction of low-dimensional materials leads to a further increase in ZT.

This confinement effect may manifest itself in Bi nanowires with a larger diameter than in conventional materials because of unusual intrinsic properties of Bi, such as a small effective mass and a large Fermi wavelength, according to eqn (2). In semimetallic Bi, the *L*-point conduction band and the *T*-point valence band should be considered with a two band model to determine the thermoelectric properties, as shown in Fig. 3(c). Therefore, to enhance the total Seebeck coefficient, the contribution of the minority carrier should be decreased, as described in the previous section. The *L*-point subband of the Bi nanowire is given by[13,15]

$$E_L(k) = -\frac{E_{gL}}{2} \pm \frac{E_{gL}}{2}\sqrt{1 + \frac{2\hbar^2}{E_{gL}}\left(\frac{{k_x}^2}{m_x} + \frac{{k_y}^2}{m_y} + \frac{{k_z}^2}{m_z}\right)}, \quad (6)$$

where E_{gL} is the band-gap energy of the *L*-point subband in bulk Bi, and the + and − signs indicate the conduction and valence bands, respectively. Therefore, the quantum confinement induced in the Bi nanowire increases the band-gap energy of the *L*-point subband as the diameter decreases, and inversely proportional to the effective mass components along the direction of confinement. Although the effect of confinement on the *T*-point subband is significantly smaller than at the *L*-point, it leads to a decrease in the band-overlap energy between the *L*-point conduction band and the *T*-point valence band, and subsequently to the SMSC transition with the band-gap opening, as shown in Fig. 3(c), right panel.[12,13] The theoretical variations of the band structure are plotted as a function of diameter in Fig. 4(a). These calculations assumed a constant effective mass and the values of the band-gap energies at the *L*- and *T*-points, band overlap energy, and Fermi energy were 36, 200, 98, and 56 meV, respectively.[17] Although the critical diameter for the SMSC transition was estimated to be 70 nm in this simple approximation, it can be corrected by taking into account the Lax two-band model, which does not assume a constant mass.[19,53] In practice, the increase in the band-gap energy of each subband causes an increase in the carrier effective

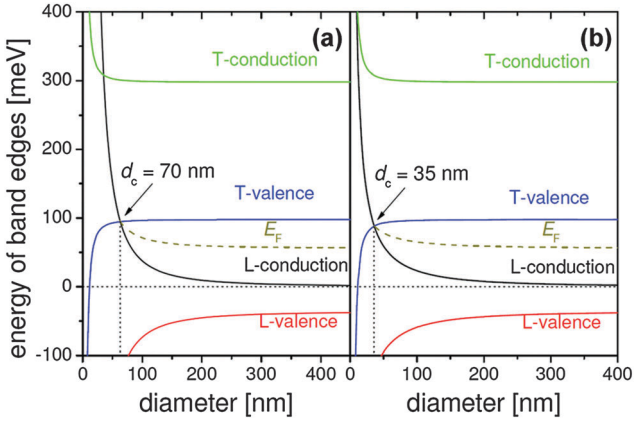

Fig. 4 Variation in the energy of each subband edge, assuming (a) a constant effective mass and (b) the Lax two-band model. The band-edge shift is dominant at the *L*-point, compared to the *T*-point. In both cases, it is due to the small electron effective mass. © 2010 Cornelius TW, Toimil-Molares ME. Originally published in InTech, Shanghai, 2010 under CC BY 3.0 license. Available from: DOI:/10.5772/39516.

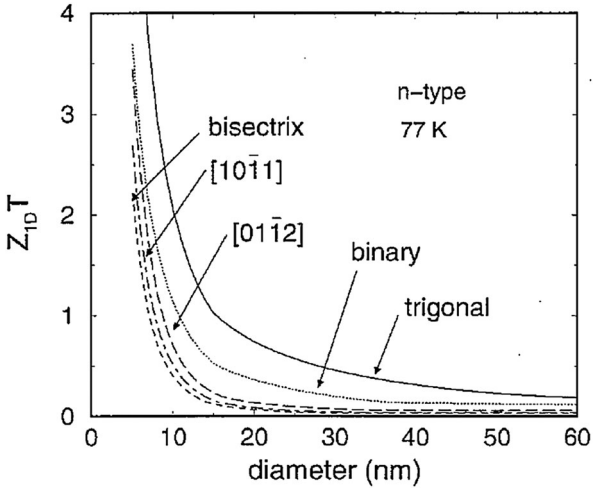

Fig. 5 Calculated *ZT* as a function of diameter for Bi nanowires oriented along different crystal directions. Reprinted with permission from The American Physical Society.[13]

mass. In Bi, the strong coupling between the valence and conduction bands at the *L*-point leads to an increase in the effective mass with increasing band gap. Consequently, the critical diameter of SMSC transition is decreased from 70 to 35 nm when using the Lax two-band model, which includes this coupling, as shown in Fig. 4(b).[17] Moreover, in addition to the coupling effect, the critical diameter also depends on the carrier effective mass and hence on the crystal direction. In a previous theoretical study, the critical diameter was calculated to be 58, 50, or 40 nm at 77 K in Bi nanowires along the trigonal, bisectrix, or binary axes, respectively.[13] Furthermore, it was found that the decrease in band-overlap energy, originating from the quantum confinement, also leads to a decrease in carrier concentration relative to bulk Bi.[13]

Fig. 5 shows the diameter-dependent *ZT* of the Bi nanowire calculated using a cylindrical potential well. The trigonal oriented nanowire shows that the maximum value and *ZT* of all the nanowires increase sharply for a diameter less than 10 nm, regardless of the crystal orientation.[13]

3. Growth and characterization of Bi nanowires

3.1 AAO template method

Array-type single-crystalline Bi nanowires were grown using anodic aluminum oxide (AAO) templates.[14,16,18–20,23–25,27–29] The AAO templates were fabricated from a high-purity Al substrate anodized in acid solutions.[54] As a result, they have a uniform porous structure that serves as a host material for Bi nanowires. The pore dimension can be controlled by the process parameters; the pore-packing density and pore diameter depend on the anodization voltage, the choice of acid solution, and the temperature. The detailed process was described elsewhere.[54] In particular, there are distinct AAO methods, involving either of two different filling mechanisms of the pores in the AAO templates: filling of liquid-phase Bi by pressurized injection[14,18,23–25,27–29] or vapor-phase Bi through the evacuated pores.[16,19,20] Fig. 6(a) shows a transmission electron microscopy (TEM) image of the AAO template with a Bi nanowire array introduced using the liquid-phase method, in which the pressurized molten Bi is injected to fill the pores, as illustrated in Fig. 6(b).[55] Although this method involves pressure to inject the Bi, we will henceforth denote it the "liquid-phase method," to distinguish it from the pressurized injection method using quartz templates, discussed below. In this method, 85–95% of the Bi nanowires were found to be

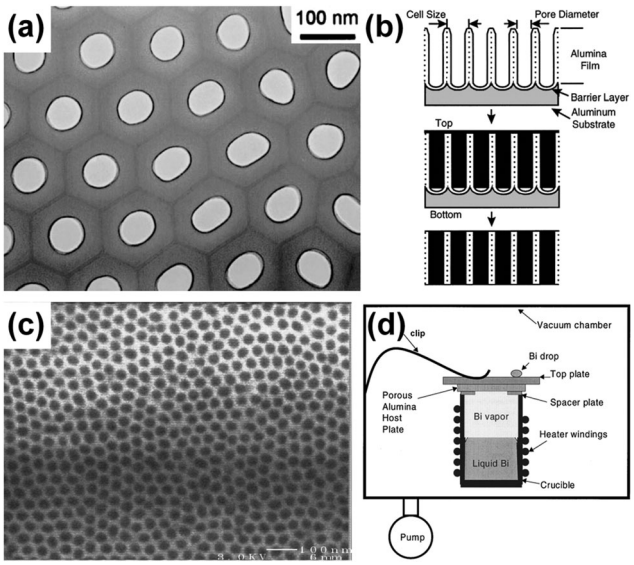

Fig. 6 Array-type Array-type Bi nanowires grown by the AAO-template method. (a) TEM image of Bi nanowires and an AAO template. (b) Growth mechanism in the liquid-phase method. (c) SEM image of Bi nanowires and an AAO template. (d) Schematic diagram of the vacuum chamber, including a crucible for growing the nanowires. Reprinted with permission form Cambridge University Press[55] and The American Physical Society.[16,59]

perpendicular to the (202) plane in the conventional hexagonal lattice system ($\vec{a}_1$, $\vec{a}_2$, and $\vec{c}$).[18,23–25,55] Bi-nanowire arrays oriented along the trigonal direction were also reported in previous studies, using this liquid-phase method.[27–29,56,57] Although the array-type Bi nanowires grown by the liquid-phase method are single-crystalline with a broad diameter range (12–109 nm),[14,55] it is difficult to grow thinner nanowires because the pressure required to inject molten Bi into the pores increases with decreasing pore diameter.[16,58] Furthermore, these nanowires experience high stress even when the external pressure is removed, owing to the confinement of the pore walls.[54] Alternatively, the vapor-phase method was developed and achieved a diameter as low as 7 nm.[16,59] Fig. 6(c) and (d) show, respectively, a scanning electron microscopy (SEM) image of Bi nanowire arrays and a schematic diagram of the vacuum chamber used, which includes a crucible for growing the nanowires.[16,59] The crystal orientations of these nanowires were found to be normal to the (202) plane in the hexagonal lattice.[11,13,16,17] The growth mechanism is described briefly below; further details are given elsewhere.[16] In the vacuum chamber, the pores of the AAO templates were evacuated and the Bi vapor was introduced into the chamber through the pores, to be heated inside the crucible. After the heater was turned off, the crucible was cooled down slowly, producing a temperature gradient within the AAO templates along the pore directions. As a result, the Bi vapor condensed inward, into the AAO templates, filling even small pores of the order of $\sim$7 nm. This method allows the study of single-crystalline Bi nanowires to be extended to a broad range of diameters (7–200 nm).[16,19,20] However, these methods using AAO templates have inherent flaws, originating from the AAO templates themselves. The high thermal conductivity of alumina can reduce the thermoelectric figure of merit of the Bi-nanowire array system; also, the four-probe measurement technique, which yields the absolute electrical conductivity of the nanowires, cannot be applied because the host material surrounds the nanowires.[28]

3.2 Ulitovsky method

The Ulitovsky method is a growth technique for obtaining an individual single-crystalline Bi nanowire, casting from the liquid phase.[26,30–32] Fig. 7 shows a cross-sectional SEM image of a Bi nanowire in a glass envelope. This method involves a two-step process. First, Bi in the borosilicate glass capsule prepared by the Ulitovsky method is heated by a high-frequency induction coil.[60] Second, the glass capsule, softened by heating, is drawn out by spooling, as shown in the inset of Fig. 7.[26,61] Although the melted Bi in the glass capsule can be discontinuous in this drawing process, it can yield a single-crystalline Bi nanowire longer than a millimeter and with a decreased diameter from 500 to 55 nm.[26,31,32] Moreover, since the molten Bi is not exposed to air in this process, a clear nanowire surface can be obtained without oxidation.[26] The crystal orientation of this nanowire was found to be in the [1−11] direction in a conventional hexagonal lattice system.[26,32,60] Although it is possible by this method to measure transport properties of an individual Bi nanowire without further surface oxidation,[24,28–30] the four-probe measurement technique is still not applicable because of the glass envelope.

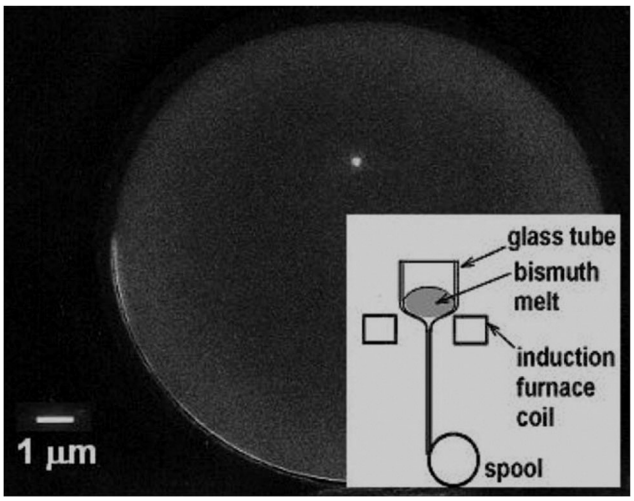

Fig. 7 A cross-sectional SEM image of a Bi nanowire grown by the Ulitovsky method. The single-crystalline Bi nanowire (white spot) is embedded within the glass tube (gray). The inset diagram outlines the growth mechanism. Reprinted with permission form The American Physical Society.[30]

3.3 Quartz template method

To investigate the thermoelectric properties with a sufficiently large temperature difference, the Bi nanowires must be longer than 1 mm and the template must have a low thermal conductivity.[34] Bi nanowires meeting these conditions were grown by pressurized injection, using a quartz template where the holes were fabricated using optical fibers, as shown in Fig. 8(a).[34–38] The pressurized injection process used in this method is similar to that used with AAO templates;[55,56] the molten Bi was injected into the holes of the quartz templates using 55 MPa argon gas.[34] As shown in Fig. 8(b), an individual single-crystalline Bi nanowire can also be grown using this method, but the injection pressure should be increased to grow thin nanowires.[36] Although the quartz-template method has some benefits, such as yielding nanowires of sufficient length, the low thermal conductivity of the template, and negligible contamination levels, the hole is too large to achieve quantum confinement. Furthermore, nanowires grown by this method were found not to have a specific crystal orientation.[38]

3.4 OFFON method

Fig. 9 shows a single-crystalline Bi nanowire grown by the OFFON method. The Bi nanowires are spontaneously grown on a Bi thin film as shown in Fig. 9(a) and (b). The method exploits the thermal stress, developed within the film that results from the mismatch in the thermal-expansion coefficients of the Bi thin film and the silicon-dioxide layer on the Si substrate.[40] During the annealing process in a vacuum after deposition of the Bi thin film (thickness $t < 50$ nm) on the Si substrate, the Bi nanowires are grown to release the induced

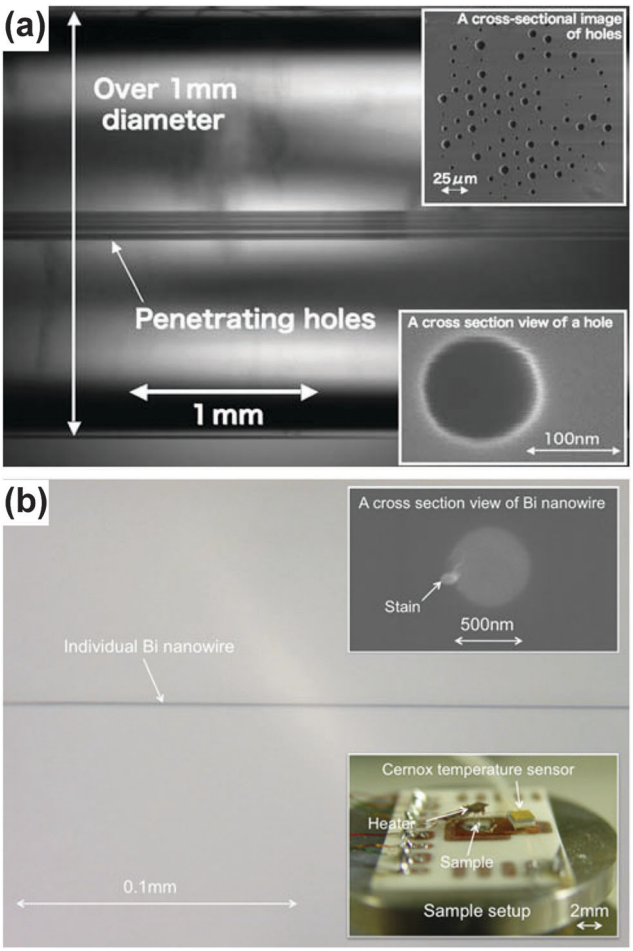

Fig. 8 Optical microscopy (OM) and SEM images of a Bi-nanowire sample grown by pressurized injection in a quartz template. Side-view OM images of (a) array type and (b) individual samples. The insets show a cross-sectional SEM image and the measurement setup. Reprinted with permission from Springer.[34,36]

thermal stress as shown in Fig. 9(c). The detailed growth process was described elsewhere.[40] In particular, the nanowire length and diameter can be controlled *via* the annealing time and the grain size of the Bi thin film, respectively (diameters of 21 nm–10 μm and lengths up to several millimeters).[44,62] Moreover, it is possible to grow Bi nanowires without host materials such as templates and avoiding contamination from chemical solutions. Magneto-[41–43] and thermoelectric[44,63] transport properties have therefore been investigated using various nanowire diameters. However, since this nanowire does not have any passivation layer on the surface, further oxidation occurs during device fabrication and the native oxide layer must be removed to allow electrical contact.[42,43] Furthermore, although the freestanding nanowire structure, in the absence of host material, is effective for measuring individual nanowires, the fabrication of an array structure for a practical thermoelectric module is challenging. The major crystal orientation of the nanowires grown by the OFFON method was found to be in the [100] direction,[44] but the minor [−102] and [001] orientations have also been confirmed.[40,62]

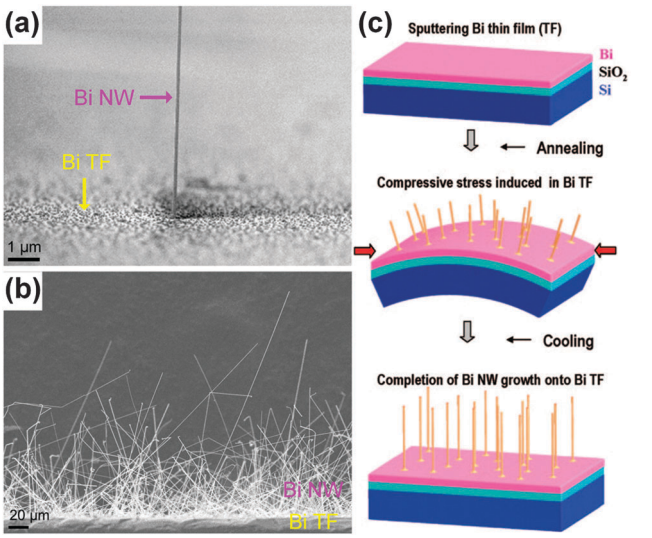

Fig. 9 Bi nanowire grown by the OFFON method. (a) and (b) SEM images of as-grown Bi nanowires on Bi thin film. (c) Schematics of the growth mechanism. Reprinted with permission from The American Chemical Society.[40]

3.5 Other methods

Other methods for obtaining low-dimensional Bi structures similar to nanowires have been reported, along with their thermoelectric properties, using electron-beam lithography (EBL)[39] and the electromigration (EM) effect.[45] SEM images of such nanowire-like Bi systems are shown in Fig. 2 (2006) and (2012), respectively. The EBL method has several advantages for investigating the thermoelectric properties of low-dimensional Bi: the position and dimension of the samples are well defined and four-probe measurements can be done.[39] However, Bi nanowires prepared by EBL are polycrystalline and do not have a completely cylindrical structure. The EM method yields low-dimensional Bi based on a [110]-oriented Bi nanowire grown by self-propulsion.[64] After the device-fabrication process, the EM effect is employed using a precisely controlled current though the nanowire to reduce the diameter, thereby producing a quantum point contact. In particular, the Seebeck coefficient measured in this structure has the highest reported value for all low-dimensional Bi to date, attaining more than 1 mV K^{-1}.[45] However, since the diameter of this structure was difficult to define owing to the point-contact structure between the nanowires, the resistivity could not be obtained. Therefore, it is impossible to evaluate the Seebeck-related enhancement reliably, and indeed to establish whether or not there is an increase in the thermoelectric performance (as determined by the power factor or *ZT*).

4. Thermoelectric properties

4.1 Electrical conductivity

Electrical conductivity is one of the parameters used to determine the thermoelectric performance (power factor) and the thermoelectric figure of merit; these quantities are proportional

to one another. The electrical conductivity σ can be deduced from measured resistance (R) of a material from the relations $\rho = R\pi(d/2)^2/L$ and $\sigma = 1/\rho$, where ρ and L are the resistivity and channel length of the material. Therefore, an accurate measurement of not only R but also the dimensions of the material is needed to determine σ. However, the diameter, length, and number of nanowires are challenging to define correctly in array-type samples using templates[14,16,27,28,34,35] and the quantum-point-contact sample using EM[45] described above. Moreover, the four-probe technique used to measure nanowire resistance only is not applicable to some individual nanowire samples that are embedded in a host material.[26,30,36–38] In practice, measurements of σ as a function of diameter in single-crystalline Bi nanowires have been performed using the OFFON method only.[44] Although the electrical conductivities of these Bi nanowires cannot be compared directly owing to this limitation, the electrical transport characteristics related to the conductivity can be determined using the temperature dependent resistance. Fig. 10 shows the resistance of the nanowires as a function of temperature. For comparison, the values are normalized by the room-temperature resistance.

In all the samples, the temperature dependence differs significantly according to the diameter, regardless of the growth method. Generally, the resistance of typical materials varies monotonically with temperature; for a typical metal (semiconductor), R decreases (increases) with decreasing temperature owing to the temperature-dependent carrier mobility (concentration). In the semimetal Bi, however, the two different dependencies coexist because of its small carrier concentration (2.7×10^{17}–3.0×10^{18} cm^{-3} at 2–300 K).[14,16,28,30] In bulk Bi, the change in carrier mobility is reportedly larger than that of the carrier concentration by more than two orders of magnitude over the temperature range 77–300 K.[14,65–67] Therefore, the mobility contribution dominates that of the concentration, resulting in a monotonic metallic temperature dependence of the resistance in bulk Bi, as shown in Fig. 10.[16] This behavior is displayed in nanowires with diameters larger than 150 nm that are grown using AAO templates and OFFON methods (Fig. 10(b) blue curve, and (d) black curve). But the rate of variation of mobility decreases with decreasing diameter owing to the non-specular surface scattering of carriers.[42] Therefore, with decreasing diameter, the resistance increases monotonically in the diameter ranges 7–65, 20–80, and 50–75 nm, for [101]- and [001]-oriented Bi nanowires grown with AAO templates and [1−11]-oriented Ulitovsky nanowires, respectively (Fig. 10(a) red, orange, dark yellow, green, and blue curves; (b) red,

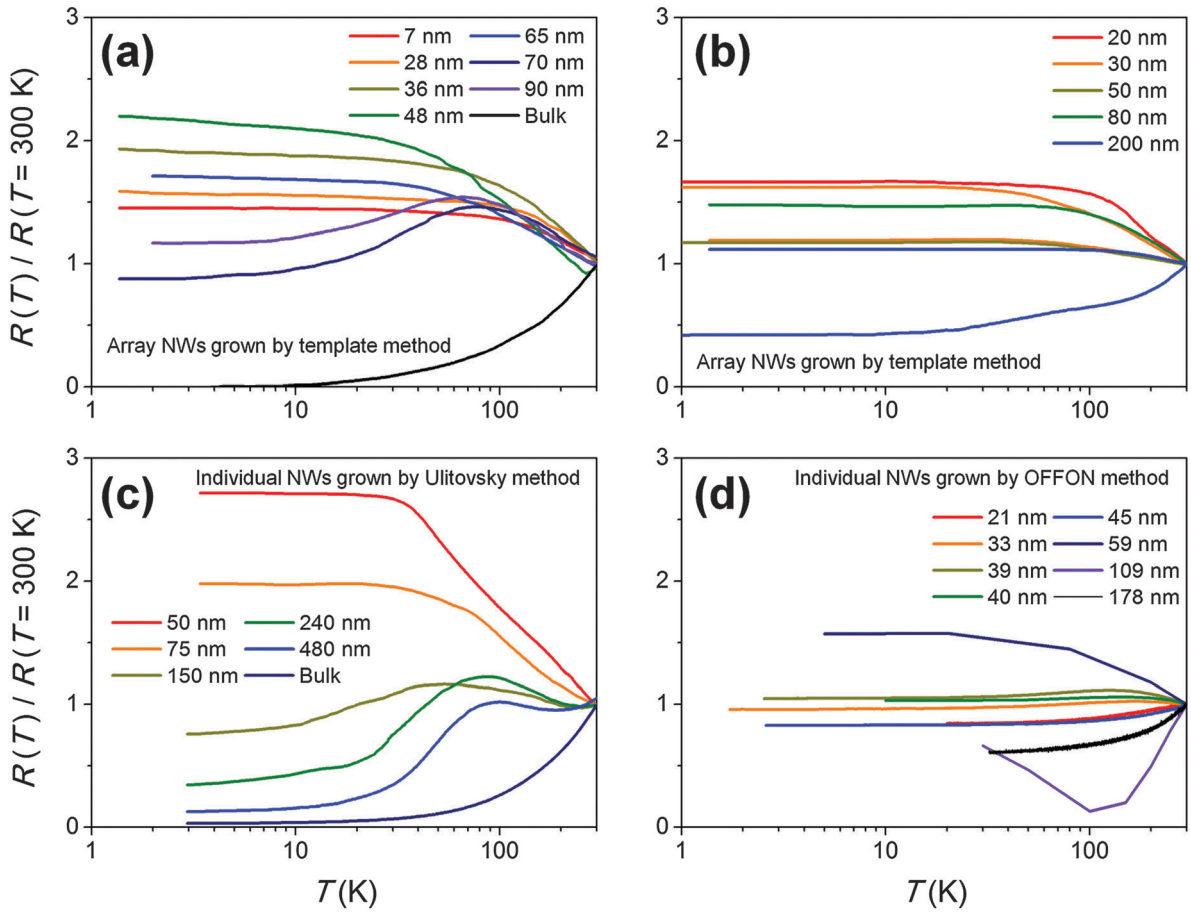

Fig. 10 Normalized temperature-dependent resistance of single-crystalline Bi nanowires oriented along (a) [101], (b) [001], (c) [1−11], and (d) [100]. The data were taken from ref. 14, 16, 26–28, 30, 42, and 44 by image digitization. The digitization errors are negligible compared to the width of the curves.

orange, dark yellow, and green curves; and (c) red and yellow curves). The 59 nm-diameter [100] OFFON nanowire also displays this monotonic increase (Fig. 10(d) dark blue curve). However, the variation in carrier concentration can also be reduced by decreasing the diameter, because the decrease in the band-overlap energy due to quantum confinement produces a decrease in carrier concentration.[13,17,43,44] As a result, the temperature-dependent resistance of Bi nanowires is determined by the complex competing trends in the temperature dependence of carrier mobility and concentration.[14,28] In this regard, the non-monotonic behavior of $R(T)$ can be reasonably well accounted for, as observed in 70 and 90 nm [101]-oriented AAO nanowires, 150, 240, and 480 nm [1−11]-oriented Ulitovsky nanowires, and 33, 39, 40, and 109 nm [100]-oriented OFFON nanowires (Fig. 10(a) dark blue and purple curves; (c) dark yellow, green, and blue curves; (d) orange, dark yellow, green, and purple curves). Consequently, in most Bi nanowires, the $R(T)$ displays three different types of behavior with decreasing diameter: as T decreases, the resistance (1) decreases monotonically according to metallic bulk behavior, (2) shows non-monotonic variation where the metallic and semiconducting characteristics coexist, and (3) increases monotonically as in a semiconductor. However, in [100] OFFON nanowires with diameters of 21 and 45 nm, $R(T)$ shows a monotonic decrease despite their small diameter, which is attributed to the large surface-carrier density (Fig. 10(d), red and blue curves).[44] Although transport behavior dominated by surface states was reported in various nanowires,[26,27] this unusual temperature-dependent resistance was observed in Bi nanowires grown by OFFON, which have a very smooth surface without an envelope material.[42,44]

The surface states are another phenomenon related to low-dimensionality in Bi. Surface states were observed by optical and transport measurements using angle-resolved photoemission spectroscopy (ARPES),[46,68] SdH oscillations,[26–29] and weak-antilocalization effects[42,69] observed in the magnetoresistance. The surface states of Bi were found to be more metallic than bulk Bi because the states overlapped the Fermi level.[46] In particular, transport properties in low-dimensional Bi are reportedly governed by the carriers originating from surface states rather than the bulk, because of the high surface-to-volume ratio.[27,69] The sheet carrier density of surface states ($n_s = 5 \times 10^{12}$ cm^{-2}), obtained by ARPES, can be converted to an effective bulk carrier density to allow comparison with the carrier concentration of bulk Bi (3.0×10^{18} cm^{-3}). We use the relation, $n = 2n_s/r$, where r is the radius of the nanowire.[14,46] This relation predicts that the carrier density induced by surface states (4.0×10^{18} cm^{-3}) can exceed that of bulk Bi for diameters less than 50 nm. Robust two-dimensional transport properties were confirmed experimentally by quantum-oscillation measurements in a 33 nm-diameter Bi nanowire, such as weak-antilocalization and universal conductance fluctuation effects;[42] the results were significantly different from those in 100- and 400 nm-diameter Bi nanowires.[41,70] Moreover, carriers induced from surface states have been found to play a significant role in defining the thermoelectric properties of Bi nanowires with small diameters, by overlapping the band gap caused by quantum confinement.[27,44]

The direct comparison of conductivities of single-crystalline Bi nanowires as a function of diameter was reported recently, based on the OFFON method.[44] With decreasing diameter, the nanowire conductivity initially retains the bulk value before decreasing strongly because spatial confinement favors non-specular surface scattering and quantum confinement produces subband shifting.[44] In particular, subband shifting was found not only to decrease carrier concentration[13] but also to increase the carrier effective mass,[43] resulting in the decrease of conductivity with decreasing diameter.[44]

4.2 Seebeck coefficient

The thermoelectric performance of a material is significantly affected by its Seebeck coefficient S, since the thermoelectric figure of merit is proportional to S^2. The Seebeck coefficient can be obtained and compared directly, regardless of the sample dimension, from the relation $S = \Delta V/\Delta T$, where ΔV and ΔT are, respectively, the differences in voltage and temperature between the ends of the sample. However, a practical measurement of S is difficult, compared to resistance, in low-dimensional materials. Especially in individual nanowires, both the formation and measurement of a temperature difference are challenging. Measurements on array-type Bi nanowires were performed using a perpendicular geometry, in which the upper and lower contacts include a heater and a thermocouple.[20,23,27] Alternatively, in the case of individual nanowires, S was measured using lateral geometric electrodes.[30] In particular, individual nanowire samples without an envelope were measured using a microheater and thermometers defined by EBL on the Si substrate.[44,45] The details of the device preparation and measurement technique were described elsewhere.[20,30,44,71]

Fig. 11 shows the Seebeck coefficient of Bi nanowires plotted as a function of temperature and diameter. Measurements in all the Bi nanowires converge to zero as the temperature approaches zero because S physically represents the entropy carried per unit charge.[72] Although S does not exceed ± 100 μV K^{-1} in any of the nanowires, the values vary significantly with the temperature, growth method, and diameter; this can be attributed to the semimetallic band structure of Bi. Eqn (1) predicts that the Seebeck coefficient is extremely sensitive to the intrinsic properties of Bi.[20,21] Because the total Seebeck coefficient was determined from the balance between negative (electrons) and positive (hole) partial Seebeck coefficients, a small change in intrinsic properties such as the carrier concentrations (n and p), carrier effective mass (m^*), or scattering time (τ), all of which contribute to the weighting factors, can change the total Seebeck coefficient significantly. Therefore, it is noted that the Seebeck coefficient of Bi nanowires can be varied by the process of sample and device preparation, as well as the crystal orientation and doping level.

All the array-type [101]- and [001]-oriented nanowires grown using the AAO template method show a negative value over most temperature ranges other than cryogenic temperatures, indicating that the majority carriers are electrons (according to eqn (1)) as shown in Fig. 10(a).[20,23,27] This behavior was also observed in array-type Sb-doped Bi nanowires.[23] In some

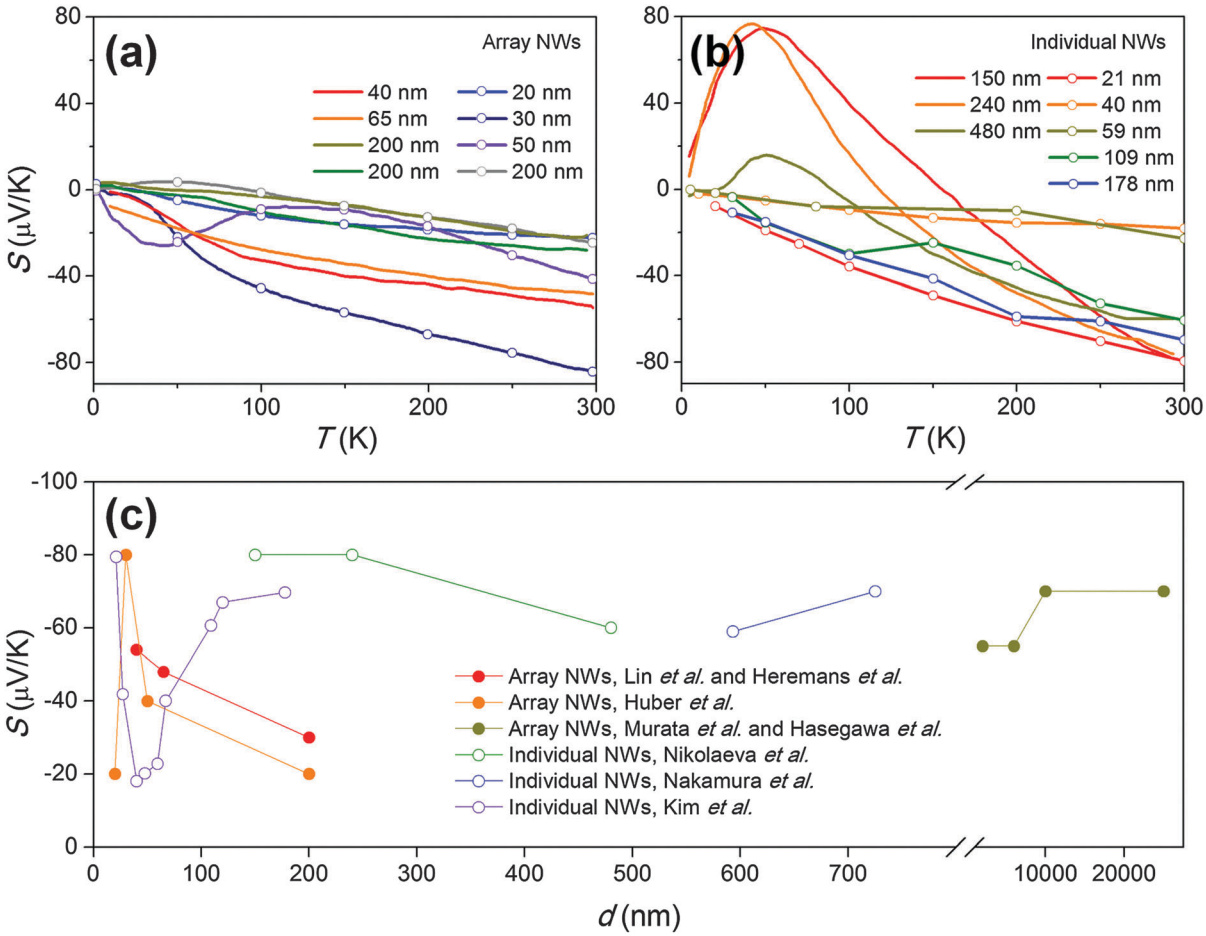

Fig. 11 Seebeck coefficient of single-crystalline Bi nanowires. (a) Temperature dependence in [101] (lines) and [001] (lines with open circles) Bi nanowires. (b) Temperature dependence in [1−11] (lines) and [100] (lines with open circles) Bi nanowires. (c) Room-temperature Seebeck coefficient as a function of diameter. The data were taken from ref. 20, 23, 27, 30, 34–37, and 44 by image digitization. Digitization errors are negligible compared to the width of the curves.

samples, the majority carriers were converted from electrons to holes below 50–100 K (Fig. 11(a) dark yellow, green, blue, and gray curves). The strong temperature dependence at low temperatures (0–30 K) in 50 nm-diameter [001]-oriented nanowires was attributed to carriers induced by surface states (Fig. 11(a) purple curve).[27] Alternatively, the Seebeck coefficients of individual [1−11]- and [100]-oriented nanowires grown by the Ulitovsky and OFFON methods indicate, respectively, stronger and weaker temperature dependences than the array-type nanowires, as shown in Fig. 11(b).[30,44] The [1−11]-oriented nanowires were especially dominated by holes over a much wider range of diameters compared to the other nanowires, with S values approaching +100 μV K^{-1} (Fig. 11(b), lines without circles). In the case of [001]-oriented nanowires, despite the relatively small variation of S with temperature compared to other nanowires, it was reported that the highest measured values for a 21 nm-nanowire originated from the carriers induced by surface states (Fig. 11(b), red curve with open circles).[44]

Fig. 11(c) represents the Seebeck coefficient for all the Bi nanowires, including those grown using quartz templates,[34–37] as a function of diameter at room temperature. Although the Seebeck coefficient for diameters larger than 200 nm is comparable to the bulk value regardless of the crystal orientation or sample preparation, the temperature dependence varies significantly with the sample type for diameters smaller than 200 nm. Some sample types indeed show opposite trends in this diameter range. This indicates that the Seebeck coefficient is more sensitive to intrinsic properties in the small-diameter regime, where quantum confinement results in subband shifting. In this regard, the change in intrinsic properties that is due to the subband shifting is estimated to be more significant than that originating from different crystal orientations or from the nanowire growth method, as reported in a previous study.[43,44] Furthermore, the predicted enhancement of S was not observed in these nanowires.[12,13] The increase in S brought about by the reduction of the diameter was demonstrated only in the quantum point contact fabricated by the EM method.[45] Although it cannot be confirmed that this increase leads to an enhancement of thermoelectric performance (in the absence of electrical-conductivity measurements), the measured value is greater than 1 mV K^{-1}.[45]

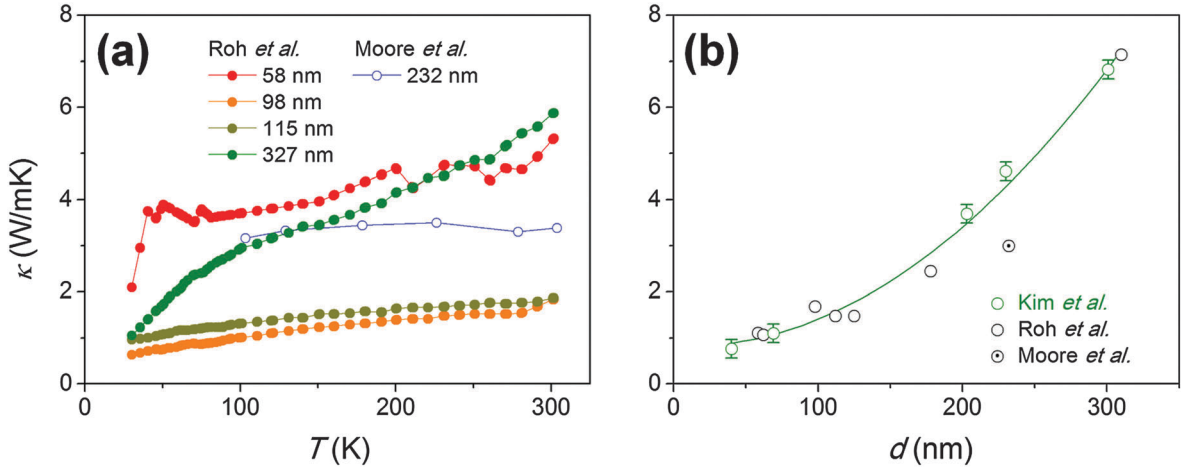

Fig. 12 Thermal conductivity of individual single-crystalline Bi nanowires. (a) Temperature dependence in [−102] (red), [100] (orange, dark yellow, and green), and [1−20] (blue) Bi nanowires. The data were taken from ref. 63 and 74 by image digitization. Digitization errors are negligible compared to the symbol size. (b) Room-temperature thermal conductivity of [100] (open circles) and [1−20] (dotted open circle) nanowires plotted as a function of diameter. Reprinted with permission form The Royal Society of Chemistry.[44]

4.3 Thermal conductivity

The thermoelectric performance of materials depends on thermal transport as well as the electrical transport. The thermoelectric figure of merit is inversely proportional to thermal conductivity. Therefore, the reduction in thermal conductivity using low-dimensional materials was intensively investigated, considering different scattering mechanisms between charge carriers and phonons.[3,73] In this regard, one-dimensional Bi is a promising thermoelectric material, not only in terms of quantum confinement but also owing to phonon scattering due to spatial confinement in the nanowire structure. However, a practical and accurate measurement of thermal conductivity in a nanowire structure is the most challenging to achieve among the three thermoelectric properties that define the thermoelectric figure of merit. In the case of charge-transport measurements, current channels in a sample are clearly defined with respect to insulating regions, such as thermally-oxidized Si substrates and air. In contrast, when measuring thermal transport, the sample must be in a thermally insulating environment (*i.e.*, a vacuum) since heat transfer must be confined to within the sample. Therefore, the Bi nanowire should be suspended from the substrate to measure the thermal conductivity accurately.[9] This is why measurements of thermal conductivity in Bi nanowires are rare, comparing to those of electrical conductivity and the Seebeck coefficient.[44,63,74] Details of the sample preparation and the measurement technique using the suspended device are given elsewhere.[44,63,74–76]

Fig. 12 shows the thermal conductivity of individual single-crystalline Bi nanowires plotted as a function of temperature or diameter. Whereas in bulk Bi aligned parallel or perpendicular to the [001] crystal orientation, the thermal conductivity was found to increase with decreasing temperature in the range 100–300 K,[77] measurements in Bi nanowires show a different behavior. The thermal conductivity of Bi nanowires grown by the OFFON method decreases with decreasing temperature (Fig. 12(a), solid circles)[63] and that grown using an AAO template shows very weak temperature dependence (Fig. 12(a), open circles).[74] It was reported that the thermal conductivity in bulk Bi is dominated by phonons at low temperatures but that charge carriers become important with increasing temperature.[78] In this regard, the temperature dependence of Bi nanowires can be understood in terms of reduced phonon propagation due to the spatial confinement.[63] The thermal conductivity of the Bi nanowires is determined by the charge-carrier component, even at low temperatures, which depends on the carrier concentration. Moreover, the thermal conductivity depends significantly on the crystal orientation. The [−102]-oriented nanowire shows higher thermal conductivity than [100] nanowires of similar diameter.[63]

Fig. 12(b) plots the room-temperature thermal conductivity of Bi nanowires as a function of their diameter. Unlike the Seebeck coefficient, the thermal conductivity shows a monotonic decrease with decreasing diameter in the range 40–300 nm. This can be attributed not only to phonon scattering but also to the fact that all the changes in intrinsic properties that are associated with the diameter decrease the charge-carrier component of thermal conductivity:[63] the concentration and mean free path of the carriers decrease and the effective mass increases.[27,43,44] Moreover, the diameter dependence depends significantly on the crystal orientation; [−102]-oriented nanowires show a stronger diameter dependence compared to [100]-oriented nanowires,[63] which was also confirmed in Bi nanowires grown using AAO templates.[74]

5. Conclusions and future outlook

In this article, we have presented a comprehensive review of single-crystalline Bi nanowires in terms of their growth methods and thermoelectric properties. Their unique intrinsic properties, highly anisotropic band structure, low band-overlap

energy, small effective mass, long mean free path, and large Fermi wavelength all make low-dimensional Bi a very promising candidate as a thermoelectric material. Single-crystalline Bi nanowires have been particularly investigated for their aptitude at displaying quantum-confinement effects more effectively than other nano-materials.

Various types of single-crystalline Bi nanowires were prepared by different methods: (1) array-type [101][18] and [001][27] oriented nanowires grown by the liquid-phase method using AAO templates, [101][16] and [1−20][74] oriented nanowires grown by the vapor-phase method using AAO templates, and nanowires grown by pressurized injection using quartz templates;[34] (2) individual [1−11]-oriented nanowires grown by the Ulitovsky method,[30] [100],[44] [−102],[62] and [001][40] nanowires grown by the OFFON method, and nanowires grown by the pressurized-injection method using quartz templates;[36] and (3) quantum-point contact fabricated by the EM method[45] based on [110]-oriented nanowires.[64] Although there was no monotonic trend in the electrical conductivity and Seebeck coefficient as a function of diameter (in all the nanowires except those grown by the OFFON and EM methods), the observed variation of the resistance and Seebeck coefficient with temperature and diameter indicates that the electrical transport properties are very sensitive to competing phenomena, owing to the semimetallic nature of the Bi band structure.[14,16,20,23,26–28,30] The decrease in band overlap energy, caused by the subband shifting for diameters below 400 nm, not only drives the SMSC transition (which would enhance the Seebeck coefficient) but also changes the intrinsic properties of the Bi nanowires.[17,43] In particular, the increase in effective mass due to the strong coupling effect caused by the subband shifting decreases the critical diameter of the SMSC transition and reduces the electrical conductivity.[17,43] Moreover, the decrease in carrier concentration and mean free path produces a further decrease in electrical conductivity with decreasing diameter. These changes in the intrinsic properties dominate the effect of SMSC transition in the total Seebeck coefficient according to eqn (1) and contribute negatively to the thermoelectric performance.[27,43,44] Furthermore, the surface states observed in low-dimensional Bi overlap with the band gap formed by the SMSC transition, so that the transport properties of Bi nanowires with diameters below 50 nm are dominated by carriers induced by the metallic surface states.[27,42,46] Conversely, the thermal conductivity is reduced monotonically with decreasing diameter, as expected. Thus, it was reported that the thermoelectric figure of merit for Bi nanowires further depends on the thermal conductivity trends rather than on the sensitive electrical conductivity and Seebeck coefficient trends.[44] Alternatively, a significant enhancement of the Seebeck coefficient was demonstrated in another low-dimensional Bi system: a quantum point contact.[45] Although the other thermoelectric properties were not confirmed, the enhancement was over two orders of magnitude relative to the bulk value. This effect was consistent with the one-band model predicted for the SMSC transition.[45]

Consequently, previous studies of the thermoelectric properties of Bi nanowires identified two major issues for achieving high-performance thermoelectric applications. First, more high-quality low-dimensional Bi nanowires are required. The enhancement of thermoelectric performance was demonstrated in a lower dimension than was predicted theoretically. To determine the thermoelectric properties accurately, the Bi nanowires should have a large aspect ratio. Second, a device-fabrication technique should be developed. The evaluation of thermoelectric performance involves three different properties (σ, S, and κ) that must be measured in the same sample. Moreover, to demonstrate a practical thermoelectric module based on nanowires, a technique to control individual nanowires is needed. Research into low-dimensional Bi has opened several possibilities for yielding high thermoelectric performance, but further development is needed to overcome the remaining obstacles to achieve practical thermoelectric energy-conversion systems.

Acknowledgements

This work was supported by the National Research Foundation of Korea (NRF) grant funded by the Korea government (MSIP) (2014R1A2A1A10053869), the Priority Research Centers Program (2009-0093823), and the Pioneer Research Center Program (2013008070).

References

1 H. J. Goldsmid, *Thermoelectric Refrigeration*, Plenum Press, New York, 1964.
2 A. Majumdar, *Science*, 2004, **303**, 777–778.
3 M. S. Dresselhaus, G. Chen, M. Y. Tang, R. G. Yang, H. Lee, D. Z. Wang, Z. F. Ren, J. P. Fleurial and P. Gogna, *Adv. Mater.*, 2007, **19**, 1043–1053.
4 G. J. Snyder and E. S. Toberer, *Nat. Mater.*, 2008, **7**, 105–114.
5 D. M. Rowe, *Thermoelectrics Handbook Macro to Nano*, CRC Press, Taylor & Francis, 2006.
6 G. D. Mahan and J. O. Sofo, *Proc. Natl. Acad. Sci. U. S. A.*, 1996, **93**, 7436–7439.
7 Y. M. Zuev, J. S. Lee, C. Galloy, H. Park and P. Kim, *Nano Lett.*, 2010, **10**, 3037–3040.
8 J. P. Heremans, V. Jovovic, E. S. Toberer, A. Saramat, K. Kurosaki, A. Charoenphakdee, S. Yamanaka and G. J. Snyder, *Science*, 2008, **321**, 554–557.
9 A. I. Hochbaum, R. Chen, R. D. Delgado, W. Liang, E. C. Garnett, M. Najarian, A. Majumdar and P. Yang, *Nature*, 2008, **451**, 163–167.
10 L. D. Hicks and M. S. Dresselhaus, *Phys. Rev. B: Condens. Matter Mater. Phys.*, 1993, **47**, 12727–12731.
11 L. D. Hicks and M. S. Dresselhaus, *Phys. Rev. B: Condens. Matter Mater. Phys.*, 1993, **47**, 16631–16634.
12 M. S. Dresselhaus, G. Dresselhaus, X. Sun, Z. Zhang, S. B. Cronin and T. Koga, *Phys. Solid State*, 1999, **41**, 679–682.
13 Y. M. Lin, X. Z. Sun and M. S. Dresselhaus, *Phys. Rev. B: Condens. Matter Mater. Phys.*, 2000, **62**, 4610–4623.
14 Z. B. Zhang, X. Z. Sun, M. S. Dresselhaus, J. Y. Ying and J. Heremans, *Phys. Rev. B: Condens. Matter Mater. Phys.*, 2000, **61**, 4850–4861.

15 S. B. Cronin, PhD thesis, Massachusetts Institute of Technology, 2002.
16 J. Heremans, C. M. Thrush, Y. M. Lin, S. Cronin, Z. Zhang, M. S. Dresselhaus and J. F. Mansfield, *Phys. Rev. B: Condens. Matter Mater. Phys.*, 2000, **61**, 2921–2930.
17 T. W. Cornelius and M. E. T. Molares, *Nanowires*, InTech, Shanghai, 2010.
18 Z. Zhang, X. Sun, M. S. Dresselhaus, J. Y. Ying and J. P. Heremans, *Appl. Phys. Lett.*, 1998, **73**, 1589–1591.
19 M. R. Black, Y. M. Lin, S. B. Cronin, O. Rabin and M. S. Dresselhaus, *Phys. Rev. B: Condens. Matter Mater. Phys.*, 2002, **65**, 195417.
20 J. Heremans and C. M. Thrush, *Phys. Rev. B: Condens. Matter Mater. Phys.*, 1999, **59**, 12579–12583.
21 J. P. Heremans, C. M. Thrush, D. T. Morelli and M.-C. Wu, *Phys. Rev. Lett.*, 2002, **88**, 216801.
22 O. Rabin, Y. M. Lin and M. S. Dresselhaus, *Appl. Phys. Lett.*, 2001, **79**, 81–83.
23 Y.-M. Lin, O. Rabin, S. B. Cronin, J. Y. Ying and M. S. Dresselhaus, *Appl. Phys. Lett.*, 2002, **81**, 2403–2405.
24 M. S. Dresselhaus, Y. M. Lin, O. Rabin and G. Dresselhaus, *Microscale Thermophys. Eng.*, 2003, **7**, 207–219.
25 Y.-M. Lin, S. B. Cronin, O. Rabin, J. Y. Ying and M. S. Dresselhaus, *Appl. Phys. Lett.*, 2001, **79**, 677–679.
26 A. Nikolaeva, D. Gitsu, L. Konopko, M. J. Graf and T. E. Huber, *Phys. Rev. B: Condens. Matter Mater. Phys.*, 2008, **77**, 075332.
27 T. E. Huber, A. Adeyeye, A. Nikolaeva, L. Konopko, R. C. Johnson and M. J. Graf, *Phys. Rev. B: Condens. Matter Mater. Phys.*, 2011, **83**, 235414.
28 T. E. Huber, A. Nikolaeva, D. Gitsu, L. Konopko, C. A. Foss and M. J. Graf, *Appl. Phys. Lett.*, 2004, **84**, 1326–1328.
29 T. E. Huber, A. Nikolaeva, L. Konopko and M. J. Graf, *Phys. Rev. B: Condens. Matter Mater. Phys.*, 2009, **79**, 201304(R).
30 A. Nikolaeva, T. E. Huber, D. Gitsu and L. Konopko, *Phys. Rev. B: Condens. Matter Mater. Phys.*, 2008, **77**, 035422.
31 A. Nikolaeva, D. Gitsu, T. Huber and L. Konopko, *Phys. Rev. B: Condens. Matter Mater. Phys.*, 2004, **346–347**, 282–286.
32 L. Konopko, T. Huber and A. Nikolaeva, *J. Low Temp. Phys.*, 2010, **159**, 253–257.
33 Y. Hasegawa, Y. Ishikawa, H. Shirai, H. Morita, A. Kurokouchi, K. Wada, T. Komine and H. Nakamura, *Rev. Sci. Instrum.*, 2005, **76**, 1–4.
34 Y. Hasegawa, M. Murata, D. Nakamura, T. Komine, T. Taguchi and S. Nakamura, *J. Electron. Mater.*, 2009, **38**, 944–949.
35 M. Murata, D. Nakamura, Y. Hasegawa, T. Komine, T. Taguchi, S. Nakamura, C. M. Jaworski, V. Jovovic and J. P. Heremans, *J. Appl. Phys.*, 2009, **105**, 113706.
36 D. Nakamura, M. Murata, Y. Hasegawa, T. Komine, D. Uematsu, S. Nakamura and T. Taguchi, *J. Electron. Mater.*, 2010, **39**, 1960–1965.
37 D. Nakamura, M. Murata, H. Yamamoto, Y. Hasegawa and T. Komine, *J. Appl. Phys.*, 2011, **110**, 053702.
38 M. Murata, F. Tsunemi, Y. Saito, K. Shirota, K. Fujiwara, Y. Hasegawa and T. Komine, *J. Electron. Mater.*, 2013, **42**, 2143–2150.
39 A. Boukai, K. Xu and J. R. Heath, *Adv. Mater.*, 2006, **18**, 864–869.
40 W. Shim, J. Ham, K. I. Lee, W. Y. Jeung, M. Johnson and W. Lee, *Nano Lett.*, 2009, **9**, 18–22.
41 W. Shim, J. Ham, J. Kim and W. Lee, *Appl. Phys. Lett.*, 2009, **95**, 232107.
42 J. Kim, S. Lee, Y. M. Brovman, M. Kim, P. Kim and W. Lee, *Appl. Phys. Lett.*, 2014, **104**, 043105.
43 J. Kim, D. Kim, T. Chang and W. Lee, *Appl. Phys. Lett.*, 2014, **105**, 123107.
44 J. Kim, S. Lee, Y. M. Brovman, P. Kim and W. Lee, *Nanoscale*, 2015, **7**, 5053–5059.
45 E. Shapira, A. Holtzman, D. Marchak and Y. Selzer, *Nano Lett.*, 2012, **12**, 808–812.
46 P. Hofmann, *Prog. Surf. Sci.*, 2006, **81**, 191–245.
47 O. Rabin, PhD thesis, Massachusetts Institute of Technology, 2004.
48 F. Y. Yang, K. Liu, K. M. Hong, D. H. Reich, P. C. Searson and C. L. Chien, *Science*, 1999, **284**, 1335–1337.
49 F. Y. Yang, K. Liu, K. Hong, D. H. Reich, P. C. Searson, C. L. Chien, Y. Leprince-Wang, K. Yu-Zhang and K. Han, *Phys. Rev. B: Condens. Matter Mater. Phys.*, 2000, **61**, 6631–6636.
50 R. T. Isaacson and G. A. Williams, *Phys. Rev.*, 1969, **185**, 682–688.
51 A. J. Levin, M. R. Black and M. S. Dresselhaus, *Phys. Rev. B: Condens. Matter Mater. Phys.*, 2009, **79**, 165117.
52 B. S. Chandrasekhar, *J. Phys. Chem. Solids*, 1959, **11**, 268–273.
53 B. Lax, J. G. Mavroides, H. J. Zeiger and R. J. Keyes, *Phys. Rev. Lett.*, 1960, **5**, 241–243.
54 Z. Zhang, D. Gekhtman, M. S. Dresselhaus and J. Y. Ying, *Chem. Mater.*, 1999, **11**, 1659–1665.
55 Z. Zhang, J. Y. Ying and M. S. Dresselhaus, *J. Mater. Res.*, 1998, **13**, 1745–1748.
56 T. E. Huber, M. J. Graf, C. A. Foss and P. Constant, *J. Mater. Res.*, 2000, **15**, 1816–1821.
57 T. E. Huber, K. Celestine and M. J. Graf, *Phys. Rev. B: Condens. Matter Mater. Phys.*, 2003, **67**, 245317.
58 M. Gurvitch, *J. Low Temp. Phys.*, 1980, **38**, 777.
59 J. Heremans, C. M. Thrush, Z. Zhang, X. Sun, M. S. Dresselhaus, J. Y. Ying and D. T. Morelli, *Phys. Rev. B: Condens. Matter Mater. Phys.*, 1998, **58**, R10091.
60 D. Gitsu, L. Konopko, A. Nikolaeva and T. E. Huber, *Appl. Phys. Lett.*, 2005, **86**, 102105.
61 A. Nikolaeva, A. Burchakov, E. Condrea and D. Gitsu, *Mater. Sci. Eng., A*, 2000, **288**, 298–302.
62 J. Ham, W. Shim, D. H. Kim, K. H. Oh, P. W. Voorhees and W. Lee, *Appl. Phys. Lett.*, 2011, **98**, 043102.
63 J. W. Roh, K. Hippalgaonkar, J. H. Ham, R. K. Chen, M. Z. Li, P. Ercius, A. Majumdar, W. Kim and W. Lee, *ACS Nano*, 2011, **5**, 3954–3960.
64 R. Sharabani, S. Reuveni, G. Noy, E. Shapira, S. Sadeh and Y. Selzer, *Nano Lett.*, 2008, **8**, 1169–1173.
65 R. Hartman, *Phys. Rev.*, 1969, **181**, 1070–1086.
66 N. Garcia and Y. H. Kao, *Phys. Lett. A*, 1968, **26**, 373–374.

67 O. P. Hansen and I. F. I. Mikhail, *Phys. Status Solidi B*, 1984, **126**, 721–728.
68 T. Hirahara, K. Miyamoto, I. Matsuda, T. Kadono, A. Kimura, T. Nagao, G. Bihlmayer, E. V. Chulkov, S. Qiao, K. Shimada, H. Namatame, M. Taniguchi and S. Hasegawa, *Phys. Rev. B: Condens. Matter Mater. Phys.*, 2007, **76**, 153305.
69 W. Ning, F. Kong, Y. Han, H. Du, J. Yang, M. Tian and Y. Zhang, *Sci. Rep.*, 2014, **4**, 7086.
70 N. Marcano, S. Sangiao, M. Plaza, L. Perez, A. F. Pacheco, R. Cordoba, M. C. Sanchez, L. Morellon, M. R. Ibarra and J. M. De Teresa, *Appl. Phys. Lett.*, 2010, **96**, 082110.
71 J. P. Small, K. M. Perez and P. Kim, *Phys. Rev. Lett.*, 2003, **91**, 256801.
72 Y. M. Zuev, W. Chang and P. Kim, *Phys. Rev. Lett.*, 2009, **102**, 096807.
73 G. Chen, *Phys. Rev. B: Condens. Matter Mater. Phys.*, 1998, **57**, 14958–14973.
74 A. L. Moore, M. T. Pettes, F. Zhou and L. Shi, *J. Appl. Phys.*, 2009, **106**, 034310.
75 D. Li, Y. Wu, P. Kim, L. Shi, P. Yang and A. Majumdar, *Appl. Phys. Lett.*, 2003, **83**, 2934–2936.
76 L. Shi, D. Li, C. Yu, W. Jang, D. Kim, Z. Yao, P. Kim and A. Majumdar, *J. Heat Transfer*, 2003, **125**, 881–888.
77 C. F. Gallo, B. S. Chandrasekhar and P. H. Sutter, *J. Appl. Phys.*, 1963, **34**, 144–152.
78 C. Uher and H. J. Goldsmid, *Phys. Status Solidi B*, 1974, **65**, 765–772.